

MINDS. The detection of ¹³CO₂ with JWST-MIRI indicates abundant CO₂ in a protoplanetary disk

SIERRA L. GRANT,¹ EWINE F. VAN DISHOCK,^{2,1} BENOÎT TABONE,³ DANNY GASMAN,⁴ THOMAS HENNING,⁵ INGA KAMP,⁶ MANUEL GÜDEL,^{7,5,8} PIERRE-OLIVIER LAGAGE,⁹ GIULIO BETTONI,¹ GIULIA PEROTTI,⁵ VALENTIN CHRISTIAENS,¹⁰ MATTHIAS SAMLAND,⁵ ADITYA M. ARABHAVI,⁶ IOANNIS ARGYRIOU,⁴ ALAIN ABERGEL,³ OLIVIER ABSIL,¹⁰ DAVID BARRADO,¹¹ ANTHONY BOCCALETTI,¹² JEROEN BOUWMAN,⁵ ALESSIO CARATTI O GARATTI,^{13,14} VINCENT GEERS,¹⁵ ADRIAN M. GLAUSER,⁸ RODRIGO GUADARRAMA,⁷ HYERIN JANG,¹⁶ JAYATEE KANWAR,^{6,17} FRED LAHUIS,¹⁸ MARIA MORALES-CALDERÓN,¹¹ MICHAEL MUELLER,⁶ CYRINE NEHMÉ,⁹ GÖRAN OLOFSSON,¹⁹ ERIC PANTIN,⁹ NICOLE PAWELLEK,⁷ TOM P. RAY,¹⁴ DONNA RODGERS-LEE,¹⁴ SILVIA SCHEITHAUER,⁵ JÜRGEN SCHREIBER,⁵ KAMBER SCHWARZ,⁵ MILOU TEMMINK,² BART VANDENBUSSCHE,⁴ MARISSA VLASBLOM,² L. B. F. M. WATERS,^{16,20} GILLIAN WRIGHT,¹⁵ LUIS COLINA,²¹ THOMAS R. GREVE,²² KAY JUSTANNONT,²³ AND GÖRAN ÖSTLIN¹⁹

¹Max-Planck Institut für Extraterrestrische Physik (MPE), Giessenbachstr. 1, 85748, Garching, Germany

²Leiden Observatory, Leiden University, 2300 RA Leiden, the Netherlands

³Université Paris-Saclay, CNRS, Institut d'Astrophysique Spatiale, 91405, Orsay, France

⁴Institute of Astronomy, KU Leuven, Celestijnenlaan 200D, 3001 Leuven, Belgium

⁵Max-Planck-Institut für Astronomie (MPIA), Königstuhl 17, 69117 Heidelberg, Germany

⁶Kapteyn Astronomical Institute, Rijksuniversiteit Groningen, Postbus 800, 9700AV Groningen, The Netherlands

⁷Dept. of Astrophysics, University of Vienna, Türkenschanzstr 17, A-1180 Vienna, Austria

⁸ETH Zürich, Institute for Particle Physics and Astrophysics, Wolfgang-Pauli-Str. 27, 8093 Zürich, Switzerland

⁹Université Paris-Saclay, Université Paris Cité, CEA, CNRS, AIM, F-91191 Gif-sur-Yvette, France

¹⁰STAR Institute, Université de Liège, Allée du Six Août 19c, 4000 Liège, Belgium

¹¹Centro de Astrobiología (CAB), CSIC-INTA, ESAC Campus, Camino Bajo del Castillo s/n, 28692 Villanueva de la Cañada, Madrid, Spain

¹²LESIA, Observatoire de Paris, Université PSL, CNRS, Sorbonne Université, Université de Paris, 5 place Jules Janssen, 92195 Meudon, France

¹³INAF – Osservatorio Astronomico di Capodimonte, Salita Moiariello 16, 80131 Napoli, Italy

¹⁴Dublin Institute for Advanced Studies, 31 Fitzwilliam Place, D02, XF86 Dublin, Ireland

¹⁵UK Astronomy Technology Centre, Royal Observatory Edinburgh, Blackford Hill, Edinburgh EH9 3HJ, UK

¹⁶Department of Astrophysics/IMAPP, Radboud University, PO Box 9010, 6500 GL Nijmegen, The Netherlands

¹⁷Space Research Institute, Austrian Academy of Sciences, Schmiedlstr. 6, A-8042, Graz, Austria

¹⁸SRON Netherlands Institute for Space Research, PO Box 800, 9700 AV, Groningen, The Netherlands

¹⁹Department of Astronomy, Stockholm University, AlbaNova University Center, 10691 Stockholm, Sweden

²⁰SRON Netherlands Institute for Space Research, Niels Bohrweg 4, NL-2333 CA Leiden, the Netherlands

²¹Centro de Astrobiología (CAB, CSIC-INTA), Carretera de Ajalvir, E-28850 Torrejón de Ardoz, Madrid, Spain

²²DTU Space, Technical University of Denmark. Building 328, Elektrovej, 2800 Kgs. Lyngby, Denmark

²³Chalmers University of Technology, Onsala Space Observatory, 439 92 Onsala, Sweden

ABSTRACT

We present JWST-MIRI MRS spectra of the protoplanetary disk around the low-mass T Tauri star GW Lup from the MIRI mid-Infrared Disk Survey (MINDS) GTO program. Emission from ¹²CO₂, ¹³CO₂, H₂O, HCN, and C₂H₂ is identified in this disk with ¹³CO₂ being detected for the first time in a protoplanetary disk. We characterize the chemical and physical conditions in the inner few au of the GW Lup disk using these molecules as probes. The spectral resolution of JWST-MIRI MRS paired with high signal-to-noise data is essential to identify these species and determine their column densities and temperatures. The Q-branches of these molecules, including those of hot-bands, are particularly sensitive to temperature and column density. We find that the ¹²CO₂ emission in the GW Lup disk is very strong and is coming from optically thick emission at a temperature of ~500 K. ¹³CO₂ is optically thinner, and tracing a larger emitting area than ¹²CO₂ and deeper into the disk based on

a lower temperature of ~ 200 K. The derived $N_{\text{CO}_2}/N_{\text{H}_2\text{O}}$ ratio of 0.25 is relatively high compared to other targets determined from *Spitzer*-IRS data. This abundance ratio may be due to an inner cavity in the gas and dust with a radius in between the H_2O and CO_2 snowlines and/or a dust trap at this location keeping water-rich icy grains from passing the water snowline. This paper demonstrates the unique ability of JWST to probe inner disk structures and chemistry through weak, previously unseen molecular features.

Keywords: protoplanetary disks – stars: pre-main sequence – stars: variables: T Tauri, Herbig Ae/Be
– planets and satellites: formation

1. INTRODUCTION

The inner 10 au of protoplanetary disks are regions of rich chemistry, with high temperatures and densities and with the snowlines of H_2O and CO_2 controlling the gas composition (Pontoppidan et al. 2014). The chemistry in this region will impact the atmospheric compositions of any exoplanets, the bulk of which are expected to form in this region (Dawson & Johnson 2018; Öberg & Bergin 2021; Mollière et al. 2022).

Of the several species that emit from the inner ~ 10 au of disks, CO_2 is a particularly informative tracer of the physical and chemical conditions in this region. In the interstellar medium, ices are rich in CO_2 (abundances of 10^{-5} with respect to the total gas density; de Graauw et al. 1996; Gibb et al. 2004; Bergin et al. 2005; Pontoppidan et al. 2008; Boogert et al. 2015). However, the CO_2 abundance in disks, derived from both LTE slab models and full disk non-LTE modeling of *Spitzer*-IRS observations, is between 10^{-9} and 10^{-7} with respect to the total gas density, indicating reprocessing in the disk (Pontoppidan & Blevins 2014; Salyk et al. 2011; Bosman et al. 2017). Despite these lower disk abundances, Pontoppidan et al. (2010) found that CO_2 was the second most common molecule detected in disks (20 disks) after water (25 disks) in a sample of 73 protoplanetary disks observed with *Spitzer*-IRS. In those sources, the CO_2 Q -branch at $14.9 \mu\text{m}$ was particularly useful as a diagnostic of the gas temperature and abundance in their inner regions. Besides ice production, CO_2 is also formed in the gas phase at moderate temperatures (100 to 200 K) through the reaction of $\text{CO} + \text{OH} \rightarrow \text{CO}_2 + \text{H}$. At higher temperatures, OH primarily reacts with H_2 to form H_2O . Thus, the $\text{CO}_2/\text{H}_2\text{O}$ ratio is sensitive to the gas temperature.

Despite the usefulness of its typically bright Q -branch, $^{12}\text{CO}_2$ is thought to be largely optically thick in the regions of the disk where it is emitting (Bosman et al. 2017). Therefore, optically thinner lines and isotologues are more useful in determining the abundance of CO_2 , as well as the physical and chemical conditions in the disk. Moderate spectral resolution and high signal-to-noise observations are needed to detect the weaker opti-

cally thin lines and isotologues, which was not possible with *Spitzer*. JWST-MIRI provides a new opportunity to study the Q -branches of $^{12}\text{CO}_2$ and $^{13}\text{CO}_2$, and the ability to identify individual P - and R -branch lines for $^{12}\text{CO}_2$.

We present JWST-MIRI observations of one of the CO_2 -bright sources identified in *Spitzer* observations: GW Lup (Pontoppidan et al. 2010; Salyk et al. 2011; Bosman et al. 2017). GW Lup (Sz 71) is an M1.5 star ($T_{\text{eff}}=3630$ K, $L_*=0.33 L_{\odot}$, $M_*=0.37 M_{\odot}$) in the Lupus I cloud at a distance of 155 pc (Alcalá et al. 2017; Andrews et al. 2018). This target was observed as part of the DSHARP survey (Andrews et al. 2018), which found a very narrow ring of continuum emission at a radius of 85 au in addition to a centrally-peaked continuum (Dullemond et al. 2018). We re-detect C_2H_2 and strong $^{12}\text{CO}_2$ emission in this disk and additionally detect $^{13}\text{CO}_2$, H_2O , HCN for the first time in this source. We fit the 13.6 to $16.3 \mu\text{m}$ wavelength range of the MIRI spectrum with local thermodynamic equilibrium (LTE) slab models to constrain the abundance and temperature for each species. We discuss our findings, in particular the detection of $^{13}\text{CO}_2$, which is the first such detection in a protoplanetary disk, and the column density ratio of CO_2 to H_2O .

2. OBSERVATIONS AND ANALYSIS

2.1. Observations and data reduction

GW Lup was observed with the Mid-InfraRed Instrument (MIRI; Rieke et al. 2015; Wells et al. 2015; Wright et al. 2015, Wright et al. submitted, Argyriou et al. in prep.) in the Medium Resolution Spectroscopy (MRS) mode on 8 August, 2022. These observations are part of the MIRI mid-Infrared Disk Survey (MINDS) JWST GTO Program (PID: 1282, PI: T. Henning). A four-point dither was performed in the positive direction. The total exposure time was 1 hour. All the JWST data used in this paper can be found in MAST: [10.17909/aes2-za93](https://mast.stsci.edu/portal/aes2-za93).

The MIRI MRS observations were processed through all three reduction stages (Bushouse et al. 2022) using Pipeline version 1.8.4. The reference files were gener-

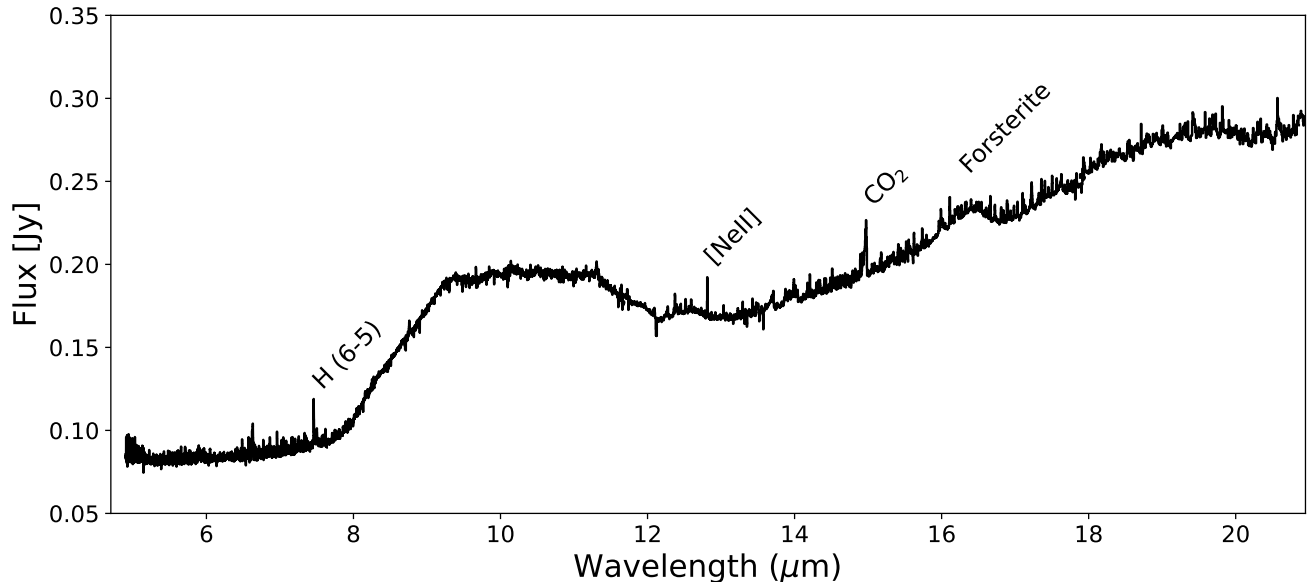


Figure 1. The JWST-MIRI MRS spectrum for GW Lup. We show all channels and sub-bands through 4A. Three of the strongest emission features are labeled. The beginning and end of each sub-band has been trimmed to reduce spurious features due to the increased noise at the ends of the bands.

ated from the observation of the reference A-type star HD 163466. Additional details on the reference files used can be found in Gasman et al. (submitted). A single dedicated point source fringe flat and dedicated spectrophotometric calibration were used in the reduction process. We skip the outlier rejection step in `Spec3`, as this produces spurious results due to the under-sampling of the PSF, causing artefacts in the extracted spectrum. Finally, a manual extraction of the spectra for each sub-band was performed, including aperture correction, with an aperture size of $2.5\lambda/D$. The correction factors are the same as those presented in Argyriou et al. (in preparation), which include the contribution of the PSF wings to the estimated background determined from an annulus around the source. The background emission from this annulus is subtracted and its value ranges from ~ 0.001 Jy in Channel 1 to ~ 0.1 Jy around $22 \mu\text{m}$.

The final GW Lup spectrum is presented in Figure 1. The $\nu_2=1-0$ $^{12}\text{CO}_2$ Q-branch is most prominent, but a large number of weaker lines are detected as well. A spurious, single-pixel spike at $18.8 \mu\text{m}$ has been removed. Below $7.5 \mu\text{m}$, the *Spitzer* low-resolution spectrum of GW Lup has a $\sim 20\%$ higher flux. However, above $7.5 \mu\text{m}$, the flux of the JWST-MIRI spectrum is $\sim 15\%$ higher than the *Spitzer*-IRS high- and low-resolution spectra of this target, but the overall shape is very similar. These offsets may be due to calibration issues and/or variability in this system. This will be in-

vestigated in a future work. In this work, we use the MIRI continuum-subtracted spectrum for analysis.

2.2. Slab Modeling Procedure

The MIRI spectrum is continuum subtracted in the 13 to $17 \mu\text{m}$ range by selecting line-free regions and using a cubic spline interpolation to determine the continuum level. This continuum is then subtracted from the observed spectra (see Section A and Figure 5).

We fit the 13 to $17 \mu\text{m}$ continuum-subtracted spectrum with local thermodynamic equilibrium (LTE) slab models. The line profile function is assumed to be Gaussian with a full width at half maximum of $\Delta V=4.7 \text{ km s}^{-1}$ ($\sigma=2 \text{ km s}^{-1}$) as is done in Salyk et al. (2011). At high optical depth, the line shape becomes a flat-topped pseudo-Gaussian due to saturation at the line core. These models allow us to reproduce the data with only three free parameters: the line of sight column density N , the gas temperature T , and the emitting area given by πR^2 for a disk of emission with radius R . While we report the emitting area in terms of this emitting radius, the emission could be coming from a ring with an area equivalent to πR^2 . We include emission from C_2H_2 , HCN, H_2O , $^{12}\text{CO}_2$, and $^{13}\text{CO}_2$. C_2H_2 and HCN line transitions are derived from the HITRAN database (Gordon et al. 2022). All the lines within 4-30 μm range are selected and are converted into LAMDA format (van der Tak et al. 2020) for compatibility with our slab model. The partition sums for these molecules are retrieved from the TIPS_2021_PYTHON package pro-

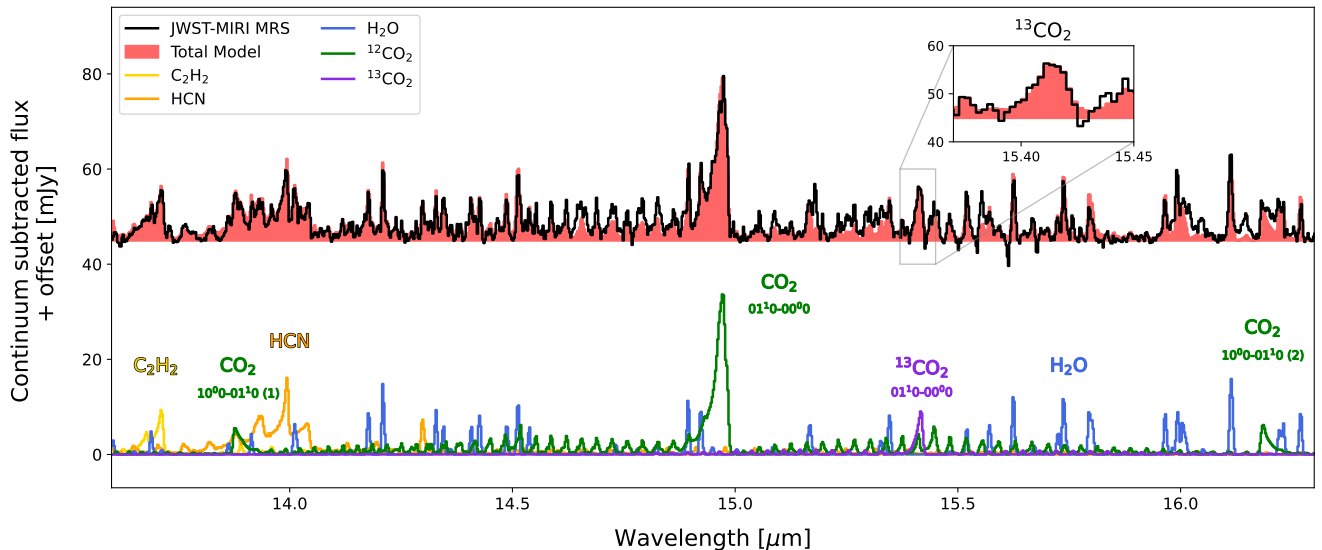


Figure 2. The 13 to 17 μm wavelength range of the GW Lup spectrum, with the JWST-MIRI data (black) compared to a model (red) composed of emission from C_2H_2 (yellow), HCN (orange), H_2O (blue), $^{12}\text{CO}_2$ (green), and $^{13}\text{CO}_2$ (purple). The inset shows a zoom-in of the $^{13}\text{CO}_2$ feature.

vided by the database¹. The H_2O data are taken from Tennyson et al. (2001). Finally, for $^{12}\text{CO}_2$ and $^{13}\text{CO}_2$, the data are those compiled by Bosman et al. (2017). We vary the emitting area, as described below, and compute a synthetic spectrum in Jy, assuming a distance to GW Lup of 155 pc. The model spectrum is then convolved to a resolving power of 2500 for Channel 3 where the emission features are present (Labiano et al. 2021). Finally, the convolved model spectrum is resampled to have the same wavelength grid as the observed spectrum.

For each molecule, a grid of models was run with N from 10^{14} to 10^{22} cm^{-2} , in steps of 0.166 in \log_{10} -space, and T from 100 to 1500 K, in steps of 25 K. The emitting area is varied by ranging the radius from 0.01 to 10 au in steps of 0.03 in \log_{10} -space. The best-fit N and T are determined using a χ^2 fit (see Appendix B and Figure 6 for more details) between the continuum subtracted data and the convolved and resampled model spectrum. For each N and T , the best-fit emitting area is determined by minimizing the χ^2 . The χ^2 fit is done in spectral windows which are selected to minimize the contribution of emission from other species while still containing features that help to constrain the fits (e.g., optically thin lines and line peaks that are sensitive to temperature). The best-fit model is found for H_2O first. This model is then subtracted from the observed, continuum-subtracted spectrum. We then fit HCN, sub-

tract that model, and continue that procedure for C_2H_2 , $^{12}\text{CO}_2$, and then the final fit is done for $^{13}\text{CO}_2$. This is illustrated, with the spectral windows used for the χ^2 determinations, in Figure 7 in Appendix B. A fixed $^{12}\text{CO}_2/^{13}\text{CO}_2$ abundance ratio of 68 is adopted based on the standard local interstellar medium ratio (Wilson & Rood 1994). The χ^2 maps are shown in Appendix B (Figure 6).

3. RESULTS

The best-fit model is presented in Figure 2 together with the continuum-subtracted spectrum in the 13.6 to 16.3 μm range. The best-fit model parameters are given in Table 1. The χ^2 maps show that at low column densities (below $\sim 10^{17}$ to 10^{18} cm^{-2} , depending on the molecule, see Figure 6), in the optically thin regime, the column density and emitting radius are completely degenerate (e.g., Salyk et al. 2011). In the optically thick regime, the emitting radius can more accurately be determined, although there is still a degeneracy between temperature and column density. Typical uncertainties can be read from the χ^2 maps where the degeneracies are also evident. The degeneracy between our three free parameters is reduced by fitting a combination of optically thick and thin lines.

3.1. $^{12}\text{CO}_2$ and $^{13}\text{CO}_2$

Our best-fitting $^{12}\text{CO}_2$ model has $N=1 \times 10^{18}$ cm^{-2} , a temperature of 475 K, and an emitting radius of 0.09 au. $^{12}\text{CO}_2$ is well constrained to a temperature below

¹ <https://hitran.org/suppl/TIPS/TIPS2021/>

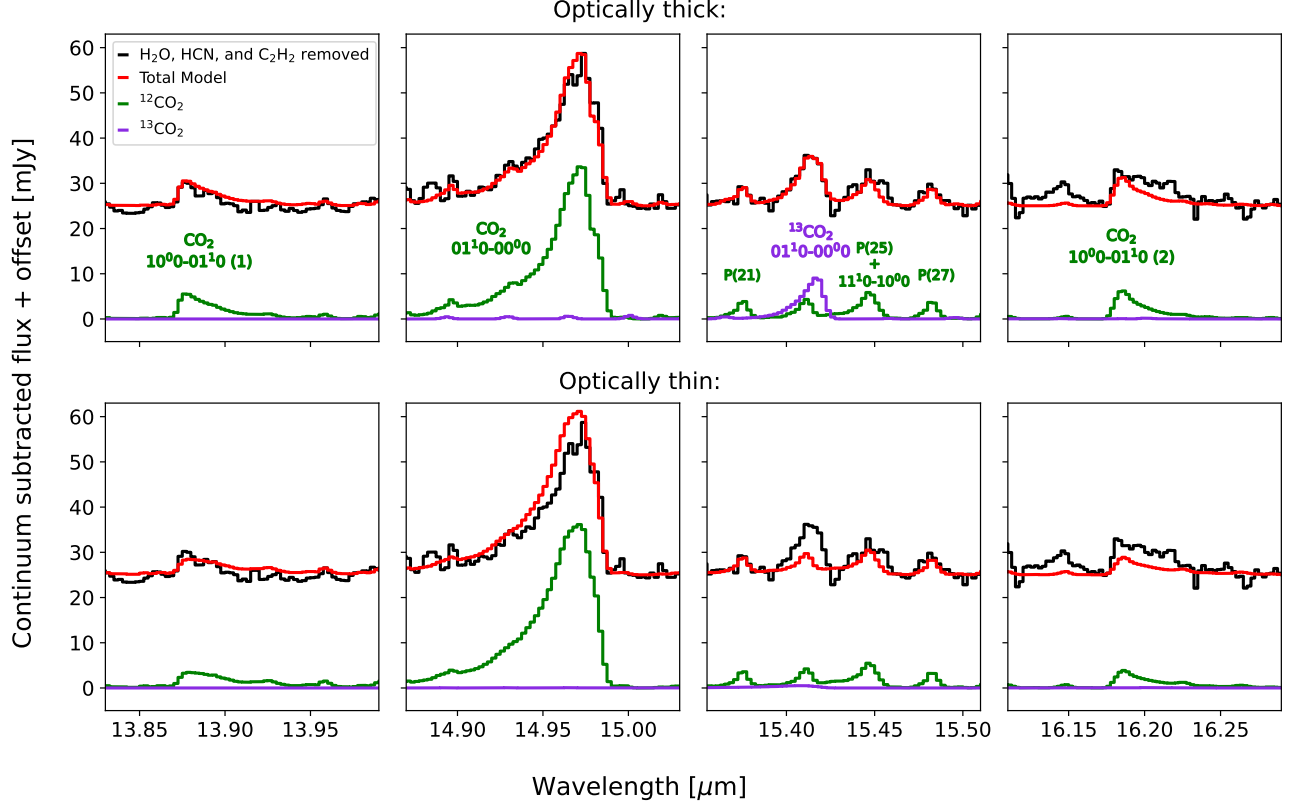


Figure 3. Zoom-ins of the $15\ \mu\text{m}$ wavelength range of GW Lup, with the JWST-MIRI data (black) compared to a model (red) composed of emission from $^{12}\text{CO}_2$ (green) and $^{13}\text{CO}_2$ (purple). The continuum and the best-fit models of C_2H_2 , HCN, and H_2O , shown in Figure 2, have been subtracted from the GW Lup spectrum. The top row shows the best optically thick fit from Figure 2, while the bottom row shows the optically thin $^{12}\text{CO}_2$ fit from Salyk et al. (2011). The optically thick model reproduces the $^{12}\text{CO}_2$ hot-band Q -branches at 13.9 and $16.2\ \mu\text{m}$ better than the optically thin model, as well as the $^{13}\text{CO}_2$ feature at $15.42\ \mu\text{m}$, assuming a $^{12}\text{CO}_2/^{13}\text{CO}_2$ ratio of 68.

~ 600 K. Using similar models and a similar technique on *Spitzer*-IRS data, Salyk et al. (2011) fit the fundamental $^{12}\text{CO}_2$ Q -branch at $14.9\ \mu\text{m}$ and find a temperature of 750 K, a column density of $1.6 \times 10^{15}\ \text{cm}^{-2}$, and an emitting radius of 1.01 au. While this optically thin model from Salyk et al. (2011) reproduces this Q -branch, it does not reproduce the $^{12}\text{CO}_2$ hot-band Q -branches at $13.9\ \mu\text{m}$ and $16.2\ \mu\text{m}$ (10^00-01^10) as well as the optically thick model does (Figure 3).

For $^{13}\text{CO}_2$, the best-fits are in the optically thin regime, wherein there is a degeneracy between the column density and emitting radius. Therefore, we adopt a $^{12}\text{CO}_2/^{13}\text{CO}_2$ ratio of 68 (Wilson & Rood 1994), which results in a $^{13}\text{CO}_2$ column density of $1 \times 10^{16}\ \text{cm}^{-2}$ and an emitting radius of 0.46 au. The $^{13}\text{CO}_2$ temperature is lower than that of $^{12}\text{CO}_2$, with the best-fit temperature of 225 K. This indicates that the optically thin $^{13}\text{CO}_2$ is indeed tracing deeper layers into the disk. The combination of $^{13}\text{CO}_2$ and the P(23) line of $^{12}\text{CO}_2$, reproduces the feature at $15.42\ \mu\text{m}$.

3.2. H_2O

We include emission from both para- and ortho- water, assuming ortho/para = 3 (e.g., van Dishoeck et al. 2021 and references therein). Many H_2O lines are present in the 13 to $17\ \mu\text{m}$ region in the GW Lup spectra, however they are weaker than the main CO_2 Q -branch and were not seen previously by *Spitzer*. An LTE slab model with a temperature of 600 K, a column density of $4 \times 10^{18}\ \text{cm}^{-2}$, and an emitting radius of 0.15 au reproduces the lines in this region. The fits at high column densities ($\gtrsim 10^{19}\ \text{cm}^{-2}$) tend to be less well constrained. This similar H_2O column density compared to CO_2 is in contrast to the much lower $\text{CO}_2/\text{H}_2\text{O}$ ratios found in the large T Tauri *Spitzer* sample by Salyk et al. (2011), which is discussed in Section 4.

3.3. Other species

For C_2H_2 and HCN (including the 02^00-01^10 HCN hot-band Q -branch at $14.3\ \mu\text{m}$), the fits point to optically thin emission, with well constrained temperatures of ~ 500 K and ~ 1000 K, respectively. This high HCN

Table 1. Best-fit model parameters

Species	N [cm^{-2}]	T [K]	R [au]
H ₂ O	4×10^{18}	600	0.15
HCN	2×10^{16}	950	0.25
C ₂ H ₂	1×10^{17}	425	0.08
¹² CO ₂	1×10^{18}	475	0.09
¹³ CO ₂	1×10^{16}	225	0.46

temperature is needed to reproduce the ratio of line peaks in the main Q -branch. The column densities for C₂H₂ and HCN are degenerate with the emitting areas/radii in this optically thin regime, although C₂H₂ is on the border between being optically thick and optically thin. The emitting area for C₂H₂ and HCN is chosen from the best-fit model, but it is only constrained such that $R \gtrsim 0.05$ au.

4. DISCUSSION

Due to its lower abundance ¹³CO₂ is more optically thin than ¹²CO₂ and is more sensitive to the total CO₂ column. The observations and best-fit models support the picture of optically thick ¹²CO₂ at higher temperatures, higher in the disk atmosphere, and optically thin ¹³CO₂ at cooler temperatures, probing deeper layers in the disk. [Bosman et al. \(2017\)](#) compare the flux of the ¹³CO₂ Q -branch at 15.42 μm to the neighboring ¹²CO₂ P(25) line at 15.45 μm , and show that this ratio is sensitive to enhancements of CO₂ at its snowline. In GW Lup, the P(25) line is stronger than the P(23) line, indicative of a contribution from the 11¹0-10⁰ hot-band Q -branch of ¹²CO₂ that is only present at high temperatures/column densities and was not seen in the models of [Bosman et al. \(2017\)](#). Therefore, the P(25) line is not a good representative of an individual P -branch line at these J -levels. Instead, the P(27) line at 15.48 μm can be used. From the best-fit models, the peak of the ¹³CO₂ Q -branch is at 7 mJy, compared to 3.8 mJy for the P(27) line. This ¹³CO₂/P(27) line ratio of 1.8 points to a low outer (10^{-8} with respect to the total gas density) and high inner (10^{-6}) disk CO₂ abundance, potentially pointing to icy pebble drift. Future modeling work will be able to confirm this.

As CO₂ and H₂O are two of the main oxygen carriers in protoplanetary disks, the relative abundances of these species is informative. While H₂O emission is present in the MIRI MRS spectrum of GW Lup, it is relatively weak compared to CO₂ with an $N_{\text{CO}_2}/N_{\text{H}_2\text{O}}$ ratio of 0.25. The large T Tauri *Spitzer* sample of [Salyk et al. \(2011\)](#) find a median $N_{\text{CO}_2}/N_{\text{H}_2\text{O}}$ ratio of 5×10^{-4} . However, the abundance ratios from [Salyk et al. \(2011\)](#)

are largely derived from the low column density and high temperature (optically thin) regime that we exclude using the weaker hot-band ¹²CO₂ Q -branches at 13.9 and 16.2 μm . Both the CO₂ and H₂O emission appear to be coming from close to the star, with best-fit emitting radii of 0.09 and 0.15 au, respectively. These radii are smaller than the estimated midplane snowline of H₂O, which is at ~ 0.3 -0.4 au for the stellar mass of GW Lup ([Mulders et al. 2015](#)).

At high temperatures ($\gtrsim 250$ K), OH will react with H₂ to form H₂O ([Glassgold et al. 2009](#)). Why then is CO₂ so abundant relative to H₂O at these temperatures and locations in this disk? We present three scenarios.

- **Pebble drift:** If dust grains coated in oxygen-rich ices are drifting inward from the outer disk, the inner disk will be enriched in oxygen ([Banzatti et al. 2020](#)). However, if this ice enrichment is taking place, both CO₂ and H₂O should be enriched. From the modeling, with H₂O at significantly higher temperatures than CO₂, it is likely that H₂O is coming from the upper layers of the disk and CO₂ closer to the midplane, but above the dust $\tau_{15\mu\text{m}}=1$ line. Indeed, [Bosman et al. \(2022\)](#) cite the detection of ¹³CO₂ as evidence for a high abundance of deep CO₂ that only exists if the H₂O abundance is low. The enrichment from ices could only explain the observed abundances if there were little vertical mixing that would transport oxygen-rich material to the disk atmosphere. There may be additional H₂O and CO₂ hidden below the dust $\tau_{15\mu\text{m}}=1$ line.
- **Photodissociation of H₂O:** If the water in the disk atmosphere is being dissociated by UV photons from the star, then the water abundance will decrease. However, this is likely not playing a large role in the case of GW Lup, as we do not detect any OH emission lines that would point to a high rate of H₂O dissociation. Additionally, the CO₂ should also be photodissociated.
- **Inner cavity and/or dust trap:** If there is an inner gas and dust cavity in the disk that extends to between the H₂O and CO₂ snowlines (estimated at ~ 0.4 and >1 au, respectively), the H₂O will be suppressed but the CO₂ will still be abundant in the gas phase. In this case, the H₂O will only be present in the uppermost layers of the disk atmosphere where the icy grains are warm enough to sublimate water ice and/or where any free volatile oxygen is driven into H₂O. Additionally, a dust trap between the snowlines, either created by the

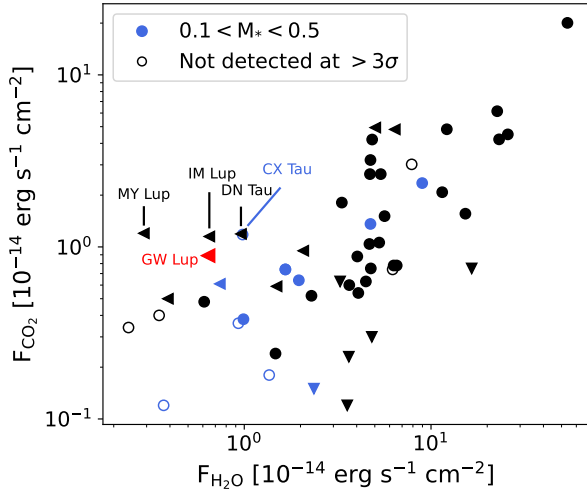


Figure 4. The *Spitzer* CO_2 vs. H_2O fluxes in the sample studied in Banzatti et al. (2020). Downward-facing triangles are those with CO_2 not detected above 3σ , left-ward facing triangles are those with H_2O not detected above 3σ , and open points are those with neither detected above 3σ . Blue points are stars with stellar masses between 0.1 and $0.5 M_\odot$, to be comparable to GW Lup (red) which has a stellar mass of $0.37 M_\odot$. We use the *Spitzer* flux for GW Lup to be consistent with the rest of the sources.

same mechanism opening the cavity or by other means, could trap water ice-rich grains from sublimating but allowing for the sublimation and enrichment of CO_2 .

Banzatti et al. (2020) (re-)determined molecular line fluxes for H_2O , HCN , C_2H_2 , and CO_2 for the *Spitzer* sample. While GW Lup has a relatively high CO_2 flux and relatively low H_2O flux compared to other disks, it is not a complete outlier (Figure 4). In order to detect $^{13}\text{CO}_2$, CO_2 needs to be abundant. Bosman et al. (2022) show that this occurs if water self-shielding is suppressed, producing more OH which is needed for additional CO_2 formation. There are several disks in the *Spitzer* survey analyzed by Pontoppidan et al. (2010), Salyk et al. (2011), and Banzatti et al. (2020) that may fall into this category: disks with low water fluxes, but high CO_2 fluxes such as DN Tau, IM Lup, MY Lup, and CX Tau (Figure 4). These also may be strong candidates for inner cavities that could be traced in the dust continuum with near-infrared interferometry or in the gas kinematics with high-spectral resolution spectroscopy, for instance, of the CO ro-vibrational lines at $4.7 \mu\text{m}$ (e.g., Brown et al. 2013; Banzatti et al. 2022). With the sensitivity and resolution of MIRI, there are likely to be other disks that will show $^{13}\text{CO}_2$ emission, which will allow us to derive strong constraints on the CO_2 abundance in these disks.

5. SUMMARY AND CONCLUSIONS

1. We identify $^{12}\text{CO}_2$, $^{13}\text{CO}_2$, H_2O , HCN , and C_2H_2 in the JWST-MIRI spectrum of GW Lup. Using LTE slab models, we reproduce the 13.6 to 16.3 μm spectrum. H_2O , HCN , and $^{13}\text{CO}_2$ are detected for the first time in this disk, as the features had line/continuum ratios that were too low to be detectable at the spectral resolution of *Spitzer*-IRS.
2. The gas-phase $^{13}\text{CO}_2$ detection is the first in a protoplanetary disk. This detection points to a high CO_2 abundance deep into the disk, with a $^{12}\text{CO}_2$ column density of $1 \times 10^{18} \text{ cm}^{-2}$, temperature of 475 K, and an emitting radius of 0.09 au.
3. The column density ratio of CO_2 to H_2O derived from LTE slab models ($N_{\text{CO}_2}/N_{\text{H}_2\text{O}}=0.25$) that fit simultaneously the $^{12}\text{CO}_2$ hot-bands, is over two orders of magnitude higher than what has previously been found in typical T Tauri disks. This may indicate an inner cavity with a radius in between the H_2O and CO_2 midplane snowlines in the disk of GW Lup.
4. While GW Lup has a relatively high CO_2 flux relative to H_2O , as seen with *Spitzer*, it is not completely an outlier, suggesting that other disks, such as those around MY Lup, IM Lup, DN Tau, and CX Tau are good candidates for the detection of $^{13}\text{CO}_2$.

Taken together, this study demonstrates that JWST MIRI-MRS has the ability to provide new and unique constraints on inner disk physical and chemical structures.

The following National and International Funding Agencies funded and supported the MIRI development: NASA; ESA; Belgian Science Policy Office (BELSPO); Centre Nationale d’Etudes Spatiales (CNES); Danish National Space Centre; Deutsches Zentrum für Luft- und Raumfahrt (DLR); Enterprise Ireland; Ministerio De Economía y Competividad; Netherlands Research School for Astronomy (NOVA); Netherlands Organisation for Scientific Research (NWO); Science and Technology Facilities Council; Swiss Space Office; Swedish National Space Agency; and UK Space Agency.

E.v.D. acknowledges support from the ERC grant 101019751 MOLDISK and the Danish National Research Foundation through the Center of Excellence “InterCat” (DNRF150). B.T. is a Laureate of the Paris Region fellowship program (which is supported

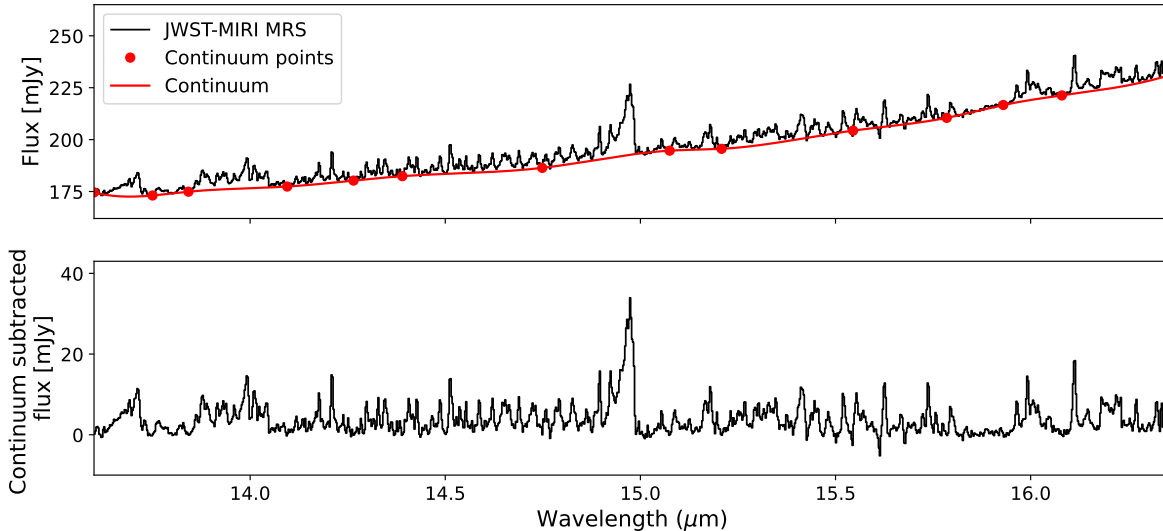


Figure 5. Top: The 13 to 17 μm wavelength range of our JWST-MIRI MRS data of GW Lup (black). The continuum points that we select are shown as the red points and the interpolated continuum is shown as the red line. Bottom: The continuum subtracted spectrum.

by the Ile-de-France Region) and has received funding under the Marie Skłodowska-Curie grant agreement No. 945298. D.G. would like to thank the Research Foundation Flanders for co-financing the present research (grant number V435622N). T.H. and K.S. acknowledge support from the ERC Advanced Grant Origins 83 24 28. I.K., A.M.A., and E.v.D. acknowledge support from grant TOP-1614.001.751 from the Dutch Research Council (NWO). I.K. and J.K. acknowledge funding from H2020-MSCA-ITN-2019, grant no. 860470 (CHAMELEON). G.B. thanks the Deutsche Forschungsgemeinschaft (DFG) - grant 138 325594231, FOR 2634/2. O.A. and V.C. acknowledge funding from the Belgian F.R.S.-FNRS. I.A. and

D.G. thank the European Space Agency (ESA) and the Belgian Federal Science Policy Office (BELSPO) for their support in the framework of the PRODEX Programme. D.B. has been funded by Spanish MCIN/AEI/10.13039/501100011033 grants PID2019-107061GB-C61 and No. MDM-2017-0737. A.C.G. has been supported by PRIN-INAF MAIN-STREAM 2017 and from PRIN-INAF 2019 (STRADE). T.P.R. acknowledges support from ERC grant 743029 EASY. D.R.L. acknowledges support from Science Foundation Ireland (grant number 21/PATH-S/9339). L.C. acknowledges support by grant PIB2021-127718NB-I00, from the Spanish Ministry of Science and Innovation/State Agency of Research MCIN/AEI/10.13039/501100011033

APPENDIX

A. CONTINUUM SUBTRACTION

The continuum is determined using a cubic spline interpolation (`scipy.interpolate.interpld`) between selected line-free regions in the spectrum (Figure 5).

B. χ^2 PROCEDURE AND MAPS

The reduced χ^2 maps for H_2O , HCN , C_2H_2 , $^{12}\text{CO}_2$, and $^{13}\text{CO}_2$ are shown in Figure 6. The reduced χ^2 is determined using the following formula:

$$\chi^2 = \frac{1}{N} \sum_{i=1}^N \frac{(F_{obs,i} - F_{mod,i})^2}{\sigma^2}, \quad (\text{B1})$$

where N is the number of resolution elements in the spectral windows that the fit is done over and σ is the standard deviation in a relatively line-free region from 15.85 to 15.94 μm (Figure 7). The contours shown in Figure 6 are the 1σ , 2σ , and 3σ levels determined as $\chi_{min}^2 + 1$, $\chi_{min}^2 + 4$, and $\chi_{min}^2 + 9$, respectively (Fedele et al. 2013). Any contribution

from other species in this line-rich region of the spectrum increases the overall χ^2 value, although the spectral windows are selected to minimize this contribution.

REFERENCES

- Alcalá, J. M., Manara, C. F., Natta, A., et al. 2017, *A&A*, 600, A20
- Andrews, S. M., Huang, J., Pérez, L. M., et al. 2018, *ApJL*, 869, L41
- Banzatti, A., Pascucci, I., Bosman, A. D., et al. 2020, *ApJ*, 903, 124
- Banzatti, A., Abernathy, K. M., Brittain, S., et al. 2022, *AJ*, 163, 174
- Bergin, E. A., Melnick, G. J., Gerakines, P. A., Neufeld, D. A., & Whittet, D. C. B. 2005, *ApJL*, 627, L33
- Boogert, A. C. A., Gerakines, P. A., & Whittet, D. C. B. 2015, *ARA&A*, 53, 541
- Bosman, A. D., Bergin, E. A., Calahan, J. K., & Duval, S. E. 2022, *ApJL*, 933, L40
- Bosman, A. D., Bruderer, S., & van Dishoeck, E. F. 2017, *A&A*, 601, A36
- Brown, J. M., Pontoppidan, K. M., van Dishoeck, E. F., et al. 2013, *ApJ*, 770, 94
- Bushouse, H., Eisenhamer, J., Dencheva, N., et al. 2022, JWST Calibration Pipeline, Zenodo, v1.7.0, Zenodo, doi:10.5281/zenodo.7038885
- Dawson, R. I., & Johnson, J. A. 2018, *ARA&A*, 56, 175
- de Graauw, T., Whittet, D. C. B., Gerakines, P. A., et al. 1996, *A&A*, 315, L345
- Dullemond, C. P., Birnstiel, T., Huang, J., et al. 2018, *ApJL*, 869, L46
- Fedele, D., Bruderer, S., van Dishoeck, E. F., et al. 2013, *A&A*, 559, A77
- Gibb, E. L., Whittet, D. C. B., Boogert, A. C. A., & Tielens, A. G. G. M. 2004, *ApJS*, 151, 35
- Glassgold, A. E., Meijerink, R., & Najita, J. R. 2009, *ApJ*, 701, 142
- Gordon, I. E., Rothman, L. S., Hargreaves, R. J., et al. 2022, *JQSRT*, 277, 107949
- Labiano, A., Argyriou, I., Álvarez-Márquez, J., et al. 2021, *A&A*, 656, A57
- Mollière, P., Molyarova, T., Bitsch, B., et al. 2022, *ApJ*, 934, 74
- Mulders, G. D., Ciesla, F. J., Min, M., & Pascucci, I. 2015, *ApJ*, 807, 9
- Öberg, K. I., & Bergin, E. A. 2021, *PhR*, 893, 1
- Pontoppidan, K. M., & Blevins, S. M. 2014, *Faraday Discussions*, 168, 49
- Pontoppidan, K. M., Salyk, C., Bergin, E. A., et al. 2014, in *Protostars and Planets VI*, ed. H. Beuther, R. S. Klessen, C. P. Dullemond, & T. Henning, 363
- Pontoppidan, K. M., Salyk, C., Blake, G. A., et al. 2010, *ApJ*, 720, 887
- Pontoppidan, K. M., Boogert, A. C. A., Fraser, H. J., et al. 2008, *ApJ*, 678, 1005
- Rieke, G. H., Wright, G. S., Böker, T., et al. 2015, *PASP*, 127, 584
- Salyk, C., Pontoppidan, K. M., Blake, G. A., Najita, J. R., & Carr, J. S. 2011, *ApJ*, 731, 130
- Tennyson, J., Zobov, N. F., Williamson, R., Polyansky, O. L., & Bernath, P. F. 2001, *Journal of Physical and Chemical Reference Data*, 30, 735
- van der Tak, F. F. S., Lique, F., Faure, A., Black, J. H., & van Dishoeck, E. F. 2020, *Atoms*, 8, 15
- van Dishoeck, E. F., Kristensen, L. E., Mottram, J. C., et al. 2021, *A&A*, 648, A24
- Wells, M., Pel, J. W., Glasse, A., et al. 2015, *PASP*, 127, 646
- Wilson, T. L., & Rood, R. 1994, *ARA&A*, 32, 191
- Wright, G. S., Wright, D., Goodson, G. B., et al. 2015, *PASP*, 127, 595

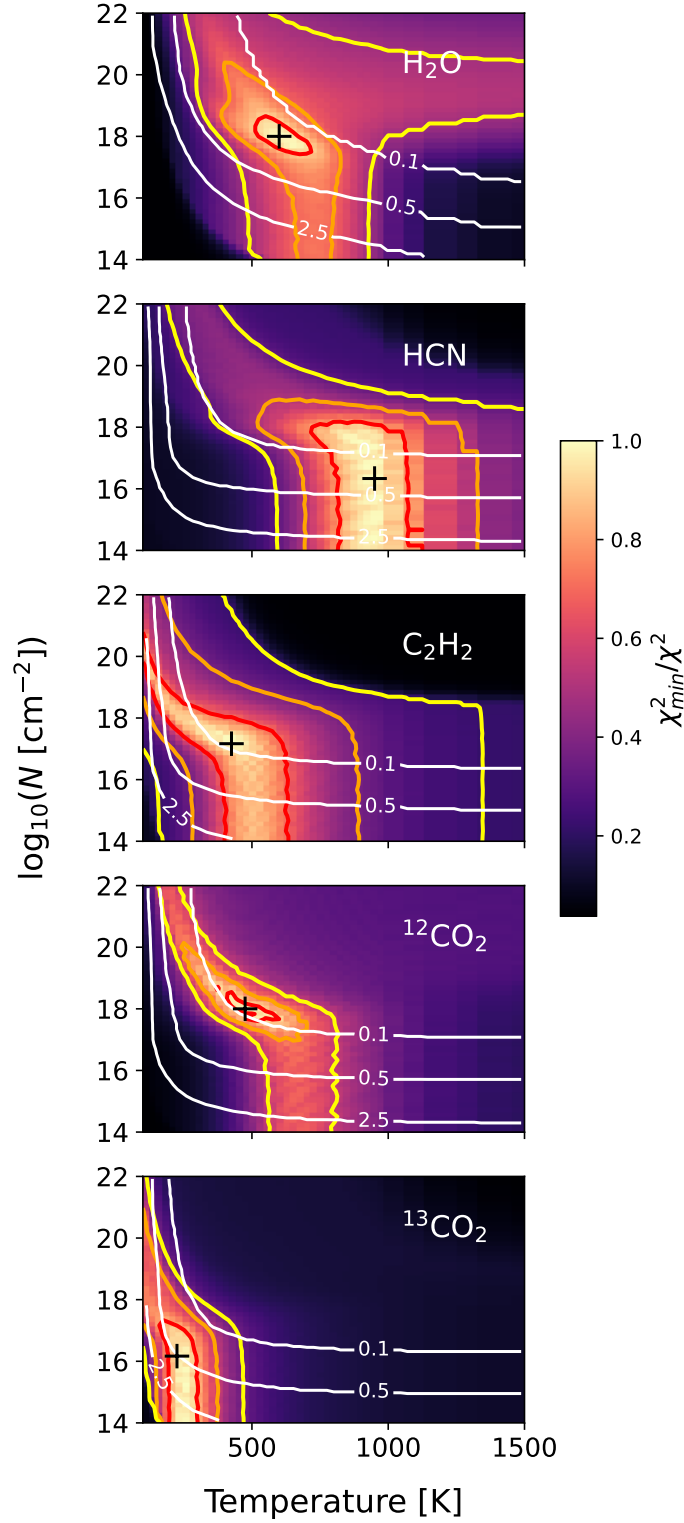


Figure 6. The χ^2 maps for H_2O , HCN , C_2H_2 , $^{12}\text{CO}_2$, and $^{13}\text{CO}_2$ (from top to bottom). The color-scale shows χ_{min}^2/χ^2 . The red, orange, and yellow contours correspond to the 1σ , 2σ , and 3σ levels. The white contours show the emitting radii in au, as given by the labels. The best-fit model is marked as the black plus. The H_2O corresponds to $p\text{H}_2\text{O}$, therefore the total H_2O column density is 4 times higher. The best-fit model corresponds to $\chi_{min}^2/\chi^2 = 1$.

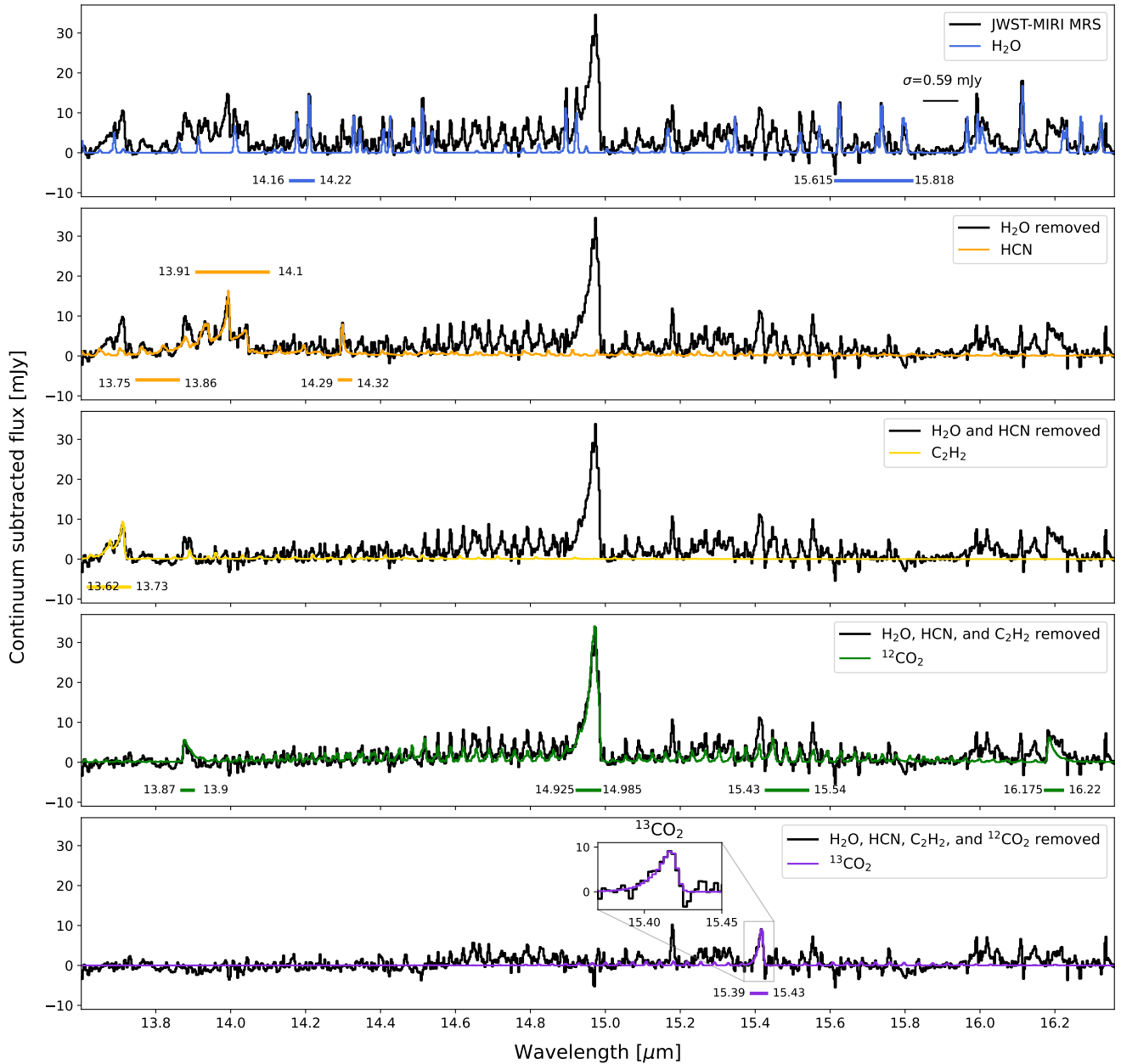


Figure 7. The best-fit model procedure is shown here. The top panel shows the best-fit H_2O model (blue) overlaid on the continuum-subtracted JWST-MIRI spectrum. In the second panel, the black spectrum is the observed spectrum after subtracting the H_2O model from the first panel. The best-fit HCN model is found using this as the input spectrum. This process continues down the panels. The spectral windows used for each species fit are shown as the horizontal bars, with the given starting and ending points. The representative noise level of the spectrum in this region, as determined by the standard deviation (0.59 mJy), is given in the top panel, determined in the relatively line-free region from 15.85 to 15.94 μm .